Supplement of Atmos. Meas. Tech., 19, 4759–4778, 2026
https://doi.org/10.5194/amt-19-4759-2026-supplement

Atmospheric Measurement Techniques
Open Access

Supplement of

The added value of new ground-based observations in improving China's methane emission quantification

Huiru Zhong et al.

Correspondence to: Lu Shen (lshen@pku.edu.cn)

Contents of this file

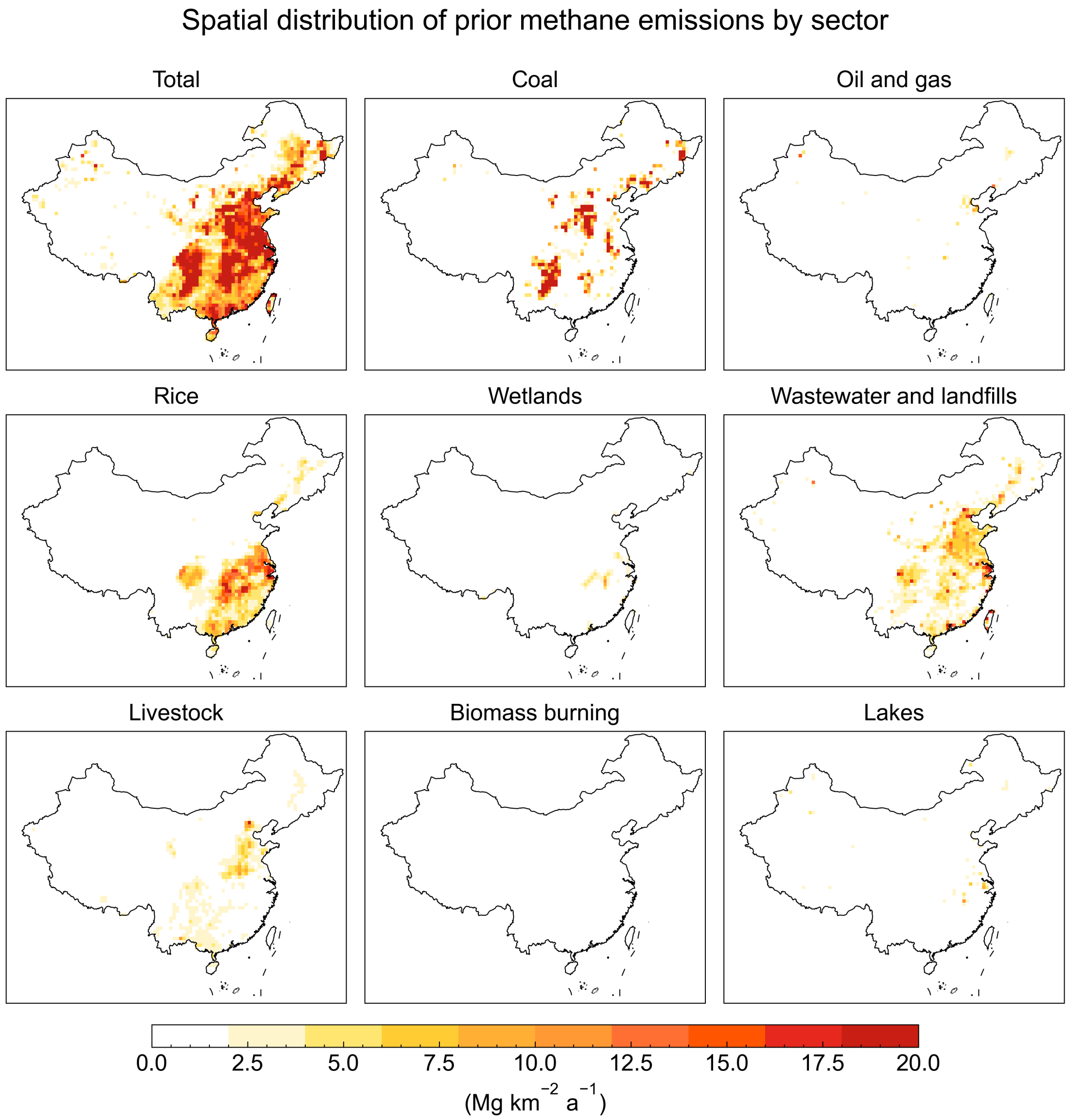

Figure S1. Spatial distribution of prior methane emissions by sector in China. Emissions for energy sectors (coal, oil and gas) are from Global Fuel Exploitation Inventory version 2.0 (GFEIv2) (Scarpelli et al., 2022). Other anthropogenic methane emissions are from Emission Database for Global Atmospheric Research (EDGARv6) inventory (Ferrario et al., 2021) and wetland methane emissions are from the mean of 18 members of the WetCHARTs v1.3.1 inventory ensemble (Ma et al., 2021). Termite methane emissions are from Fung et al., (Fung et al., 1991), and aquatic system methane emissions are from Johnson et al., (Johnson et al., 2022). EDGAR data © European Commission, Joint Research Centre (JRC). WetCHARTs data © NASA/JPL and partners.

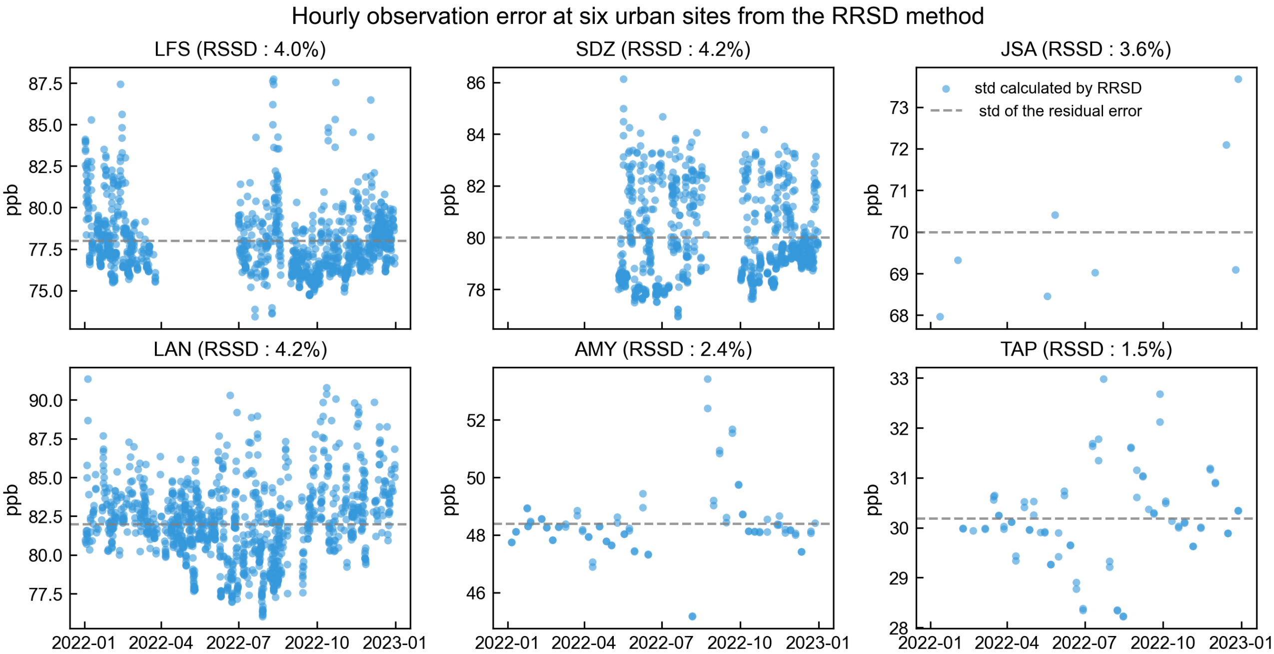

Figure S2. Hourly error at six existing urban stations derived from the relative residual standard deviation (RRSD) method. Gray dashed lines represent the standard deviation of the residual error. Blue dots denote the observation-specific error standard deviations calculated using the RRSD method (see Section 2.4 for details).

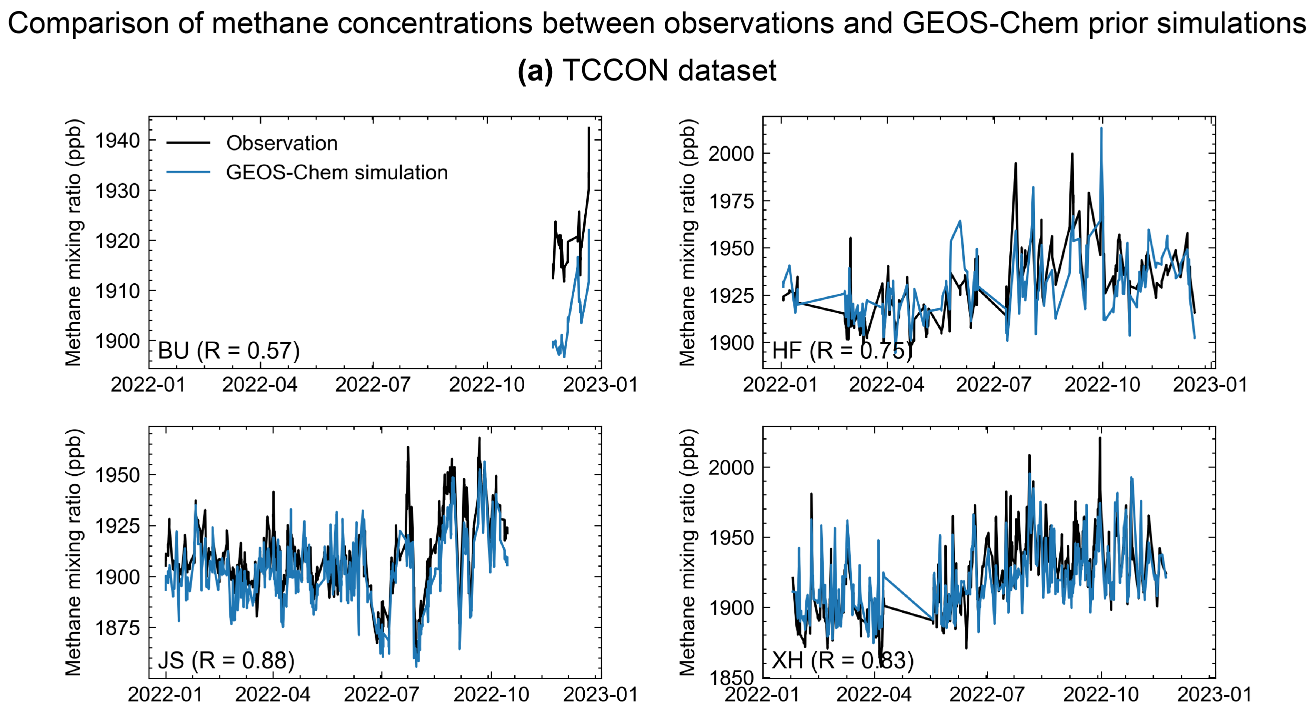

Figure S3. Comparison of methane concentrations between observations and GEOS-Chem prior simulations. Methane observations (ppb) from **(a)** TCCON XCH_4 and **(b)** ObsPack v7.0 surface CH_4 concentrations. The lower-left corner of each panel indicates the correlation coefficient between the observations and the simulations. (Continued on next page.)

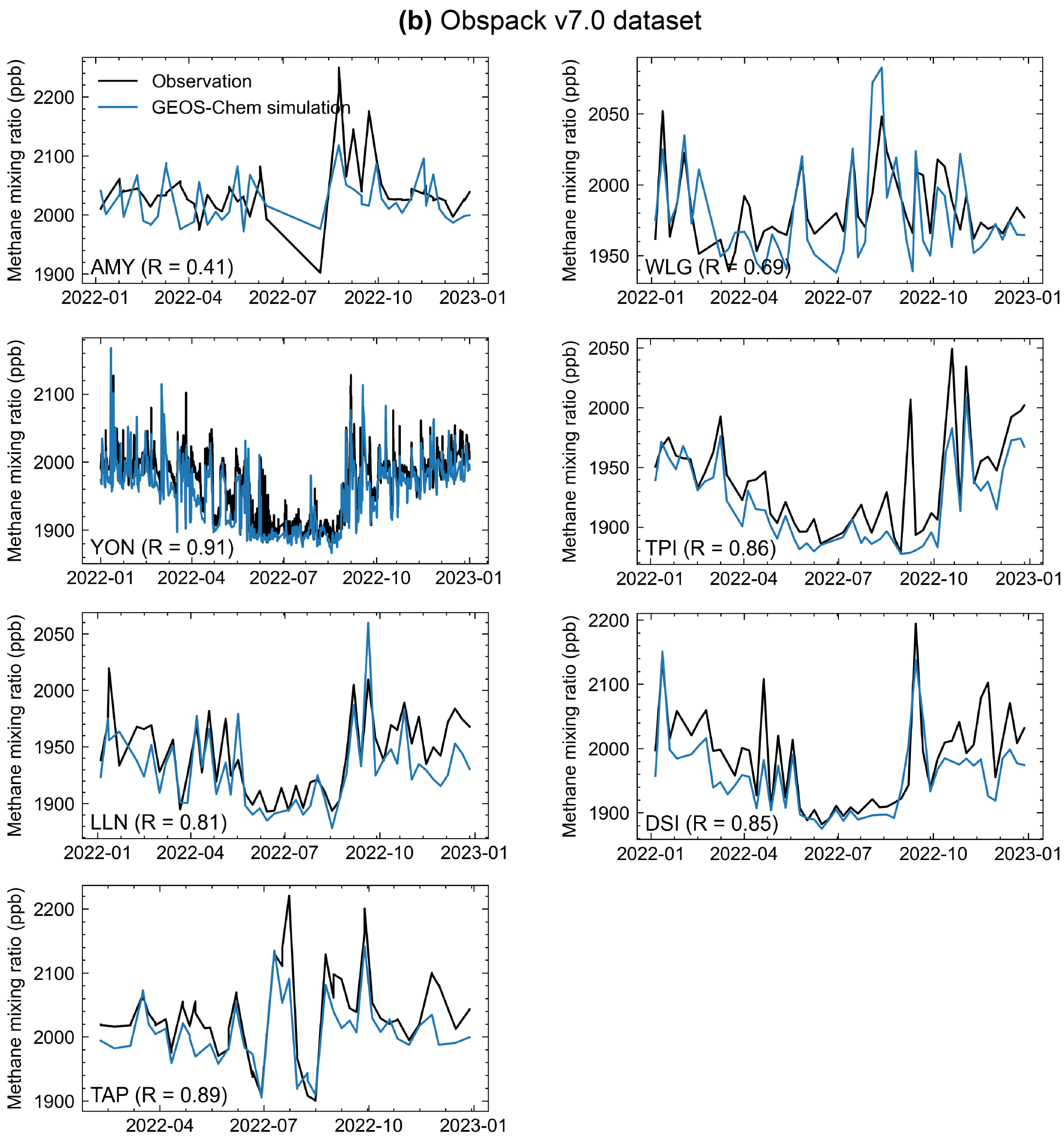

Figure S3. (continued).

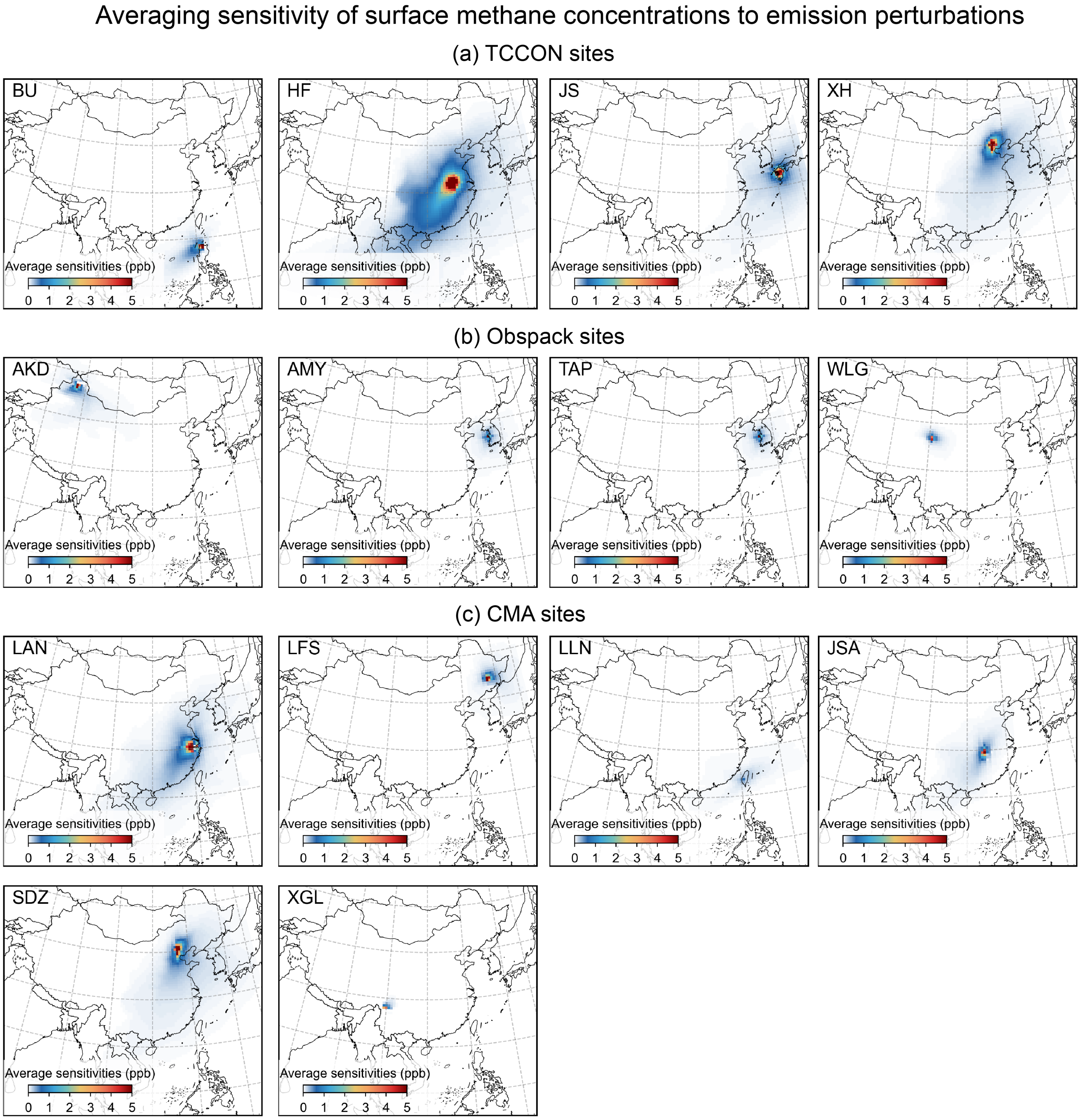

Figure S4. Hourly averaged sensitivities (Jacobians) of surface methane concentrations to localized emission perturbations. Sensitivities are derived from GEOS-Chem simulations by perturbing emissions and computing the concentration changes. Note that for maritime sites (e.g., YON, DSI and TPI), the absence of prior emissions within their respective state vector precludes direct local perturbation. However, these sites provide essential constraints on upwind emissions from adjacent terrestrial regions via regional transport.

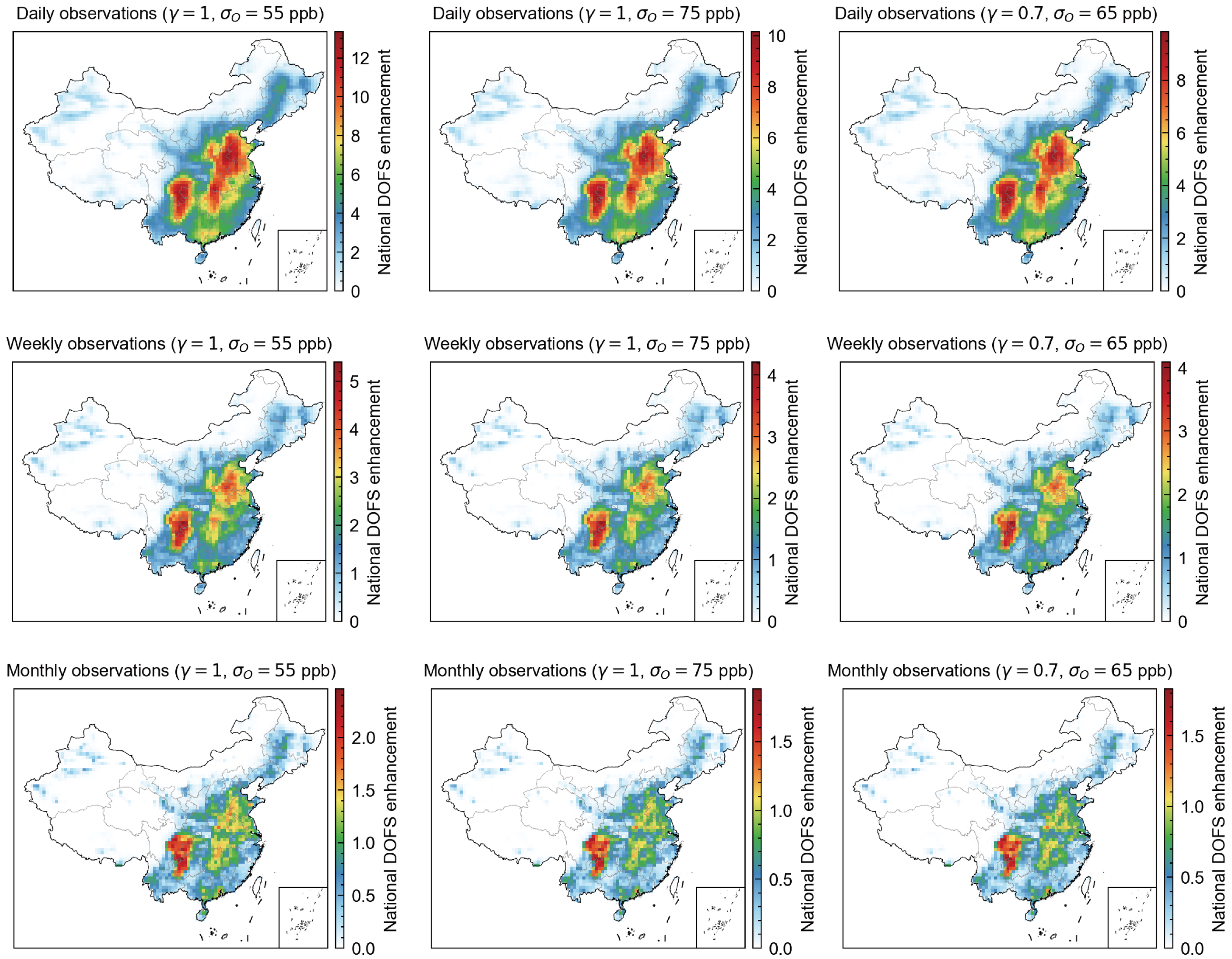

Figure S5. The degrees of freedom for signal (DOFS) enhancement in China by adding one ground station with different temporal frequencies and parameter selection in the inversion. The results are evaluated under different configurations of the regularization factor (γ = 0.7 and 1) and observation error standard deviations (σ_O= 55, 65 and 75 ppb).

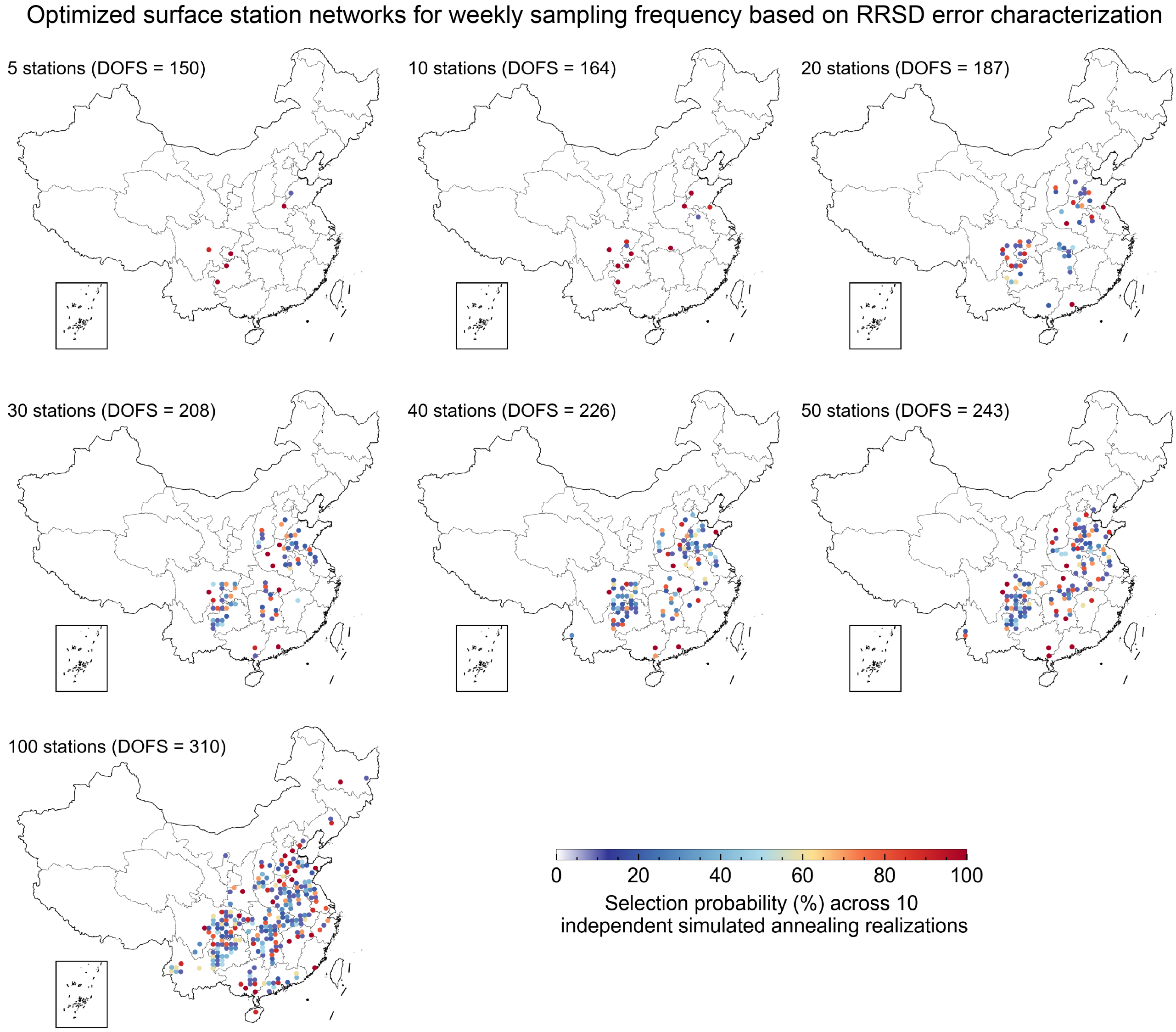

Figure S6. Optimized network expansion under weekly sampling when observation error is calculated by the relative residual standard deviation (RRSD) method. Panels show the selection probability (%) of each grid cell for a new site across 10 independent simulated annealing realizations, for network expansions of 5 to 100 new sites. The corresponding increase in the degrees of freedom for signal (DOFS) is displayed within each panel.

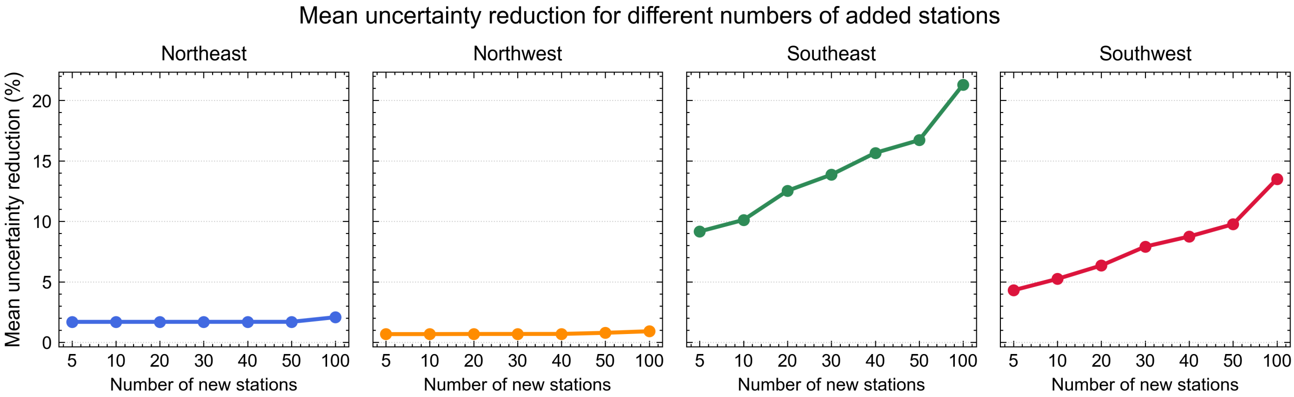

Figure S7. Regional mean uncertainty reduction contributed by the existing observational network and the addition of new surface sites. The hypothetical new stations (ranging from 5 to 100) are assumed to have a fixed weekly sampling frequency.

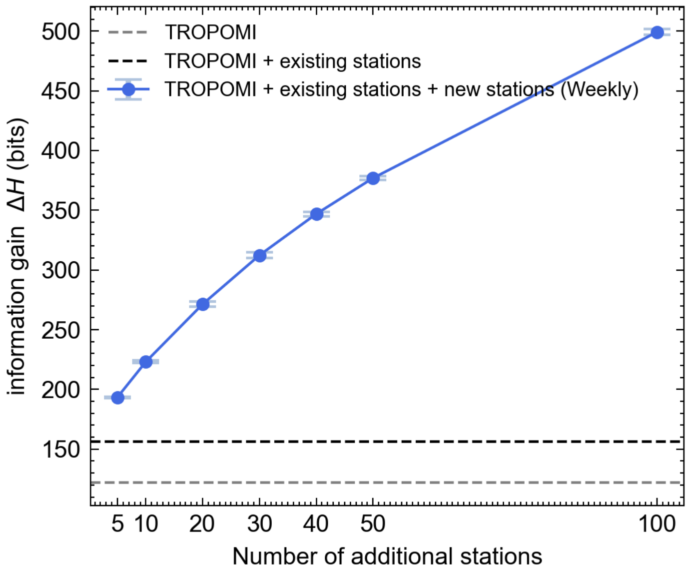

Figure S8. The information gain (ΔH) over China for different observational network configurations. The gray dashed line represents the information gain from TROPOMI observations alone, and the black dashed line represents TROPOMI combined with the existing surface network. Blue circles show the information gain after further adding hypothetical surface stations (with weekly sampling frequency), with *x*-axis indicating the number of additional stations. Error bars denote the 95% confidence intervals derived from 50 independent simulated annealing experiments.

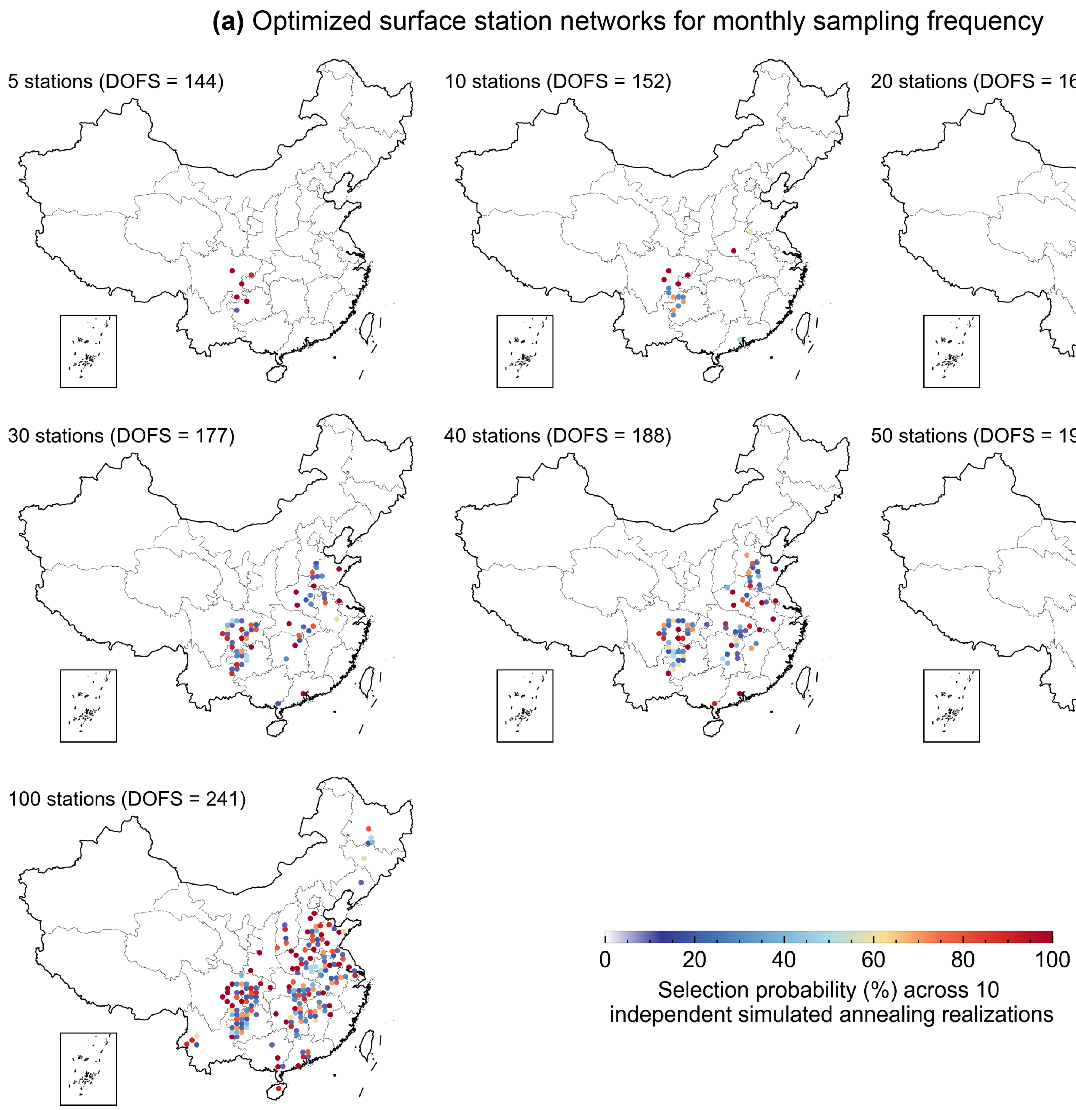

Figure S9. Optimized surface station networks for monthly and daily sampling frequencies. **(a)** Monthly sampling frequency. **(b)** Daily sampling frequency. The panels show the selection probability (%) of each grid cell for a new site across 10 independent simulated annealing realizations, spanning network sizes of 5 to 100 new stations. The corresponding increase in the degrees of freedom for signal (DOFS) is displayed within each panel. (Continued on next page)

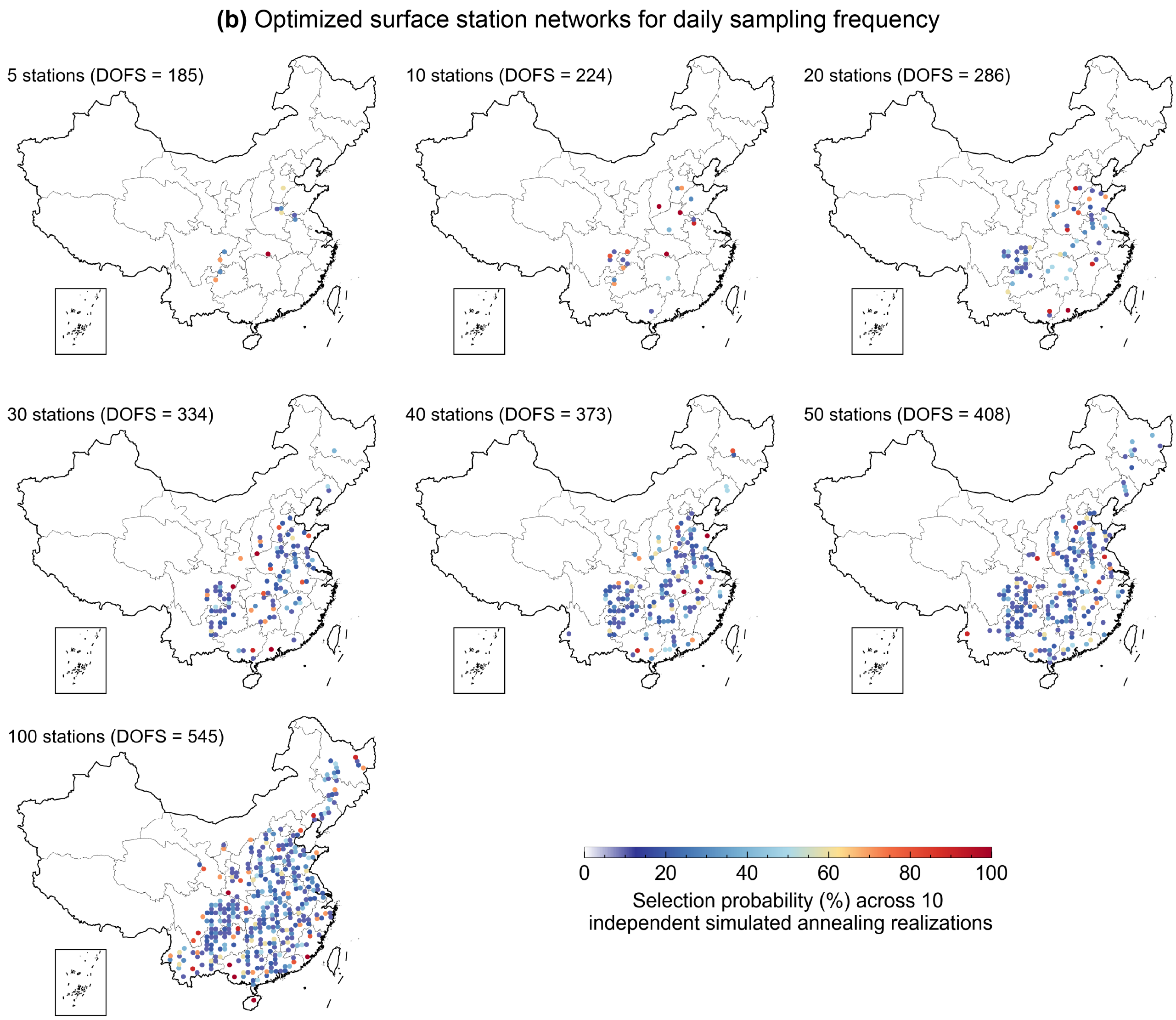

Figure S9. (continued).

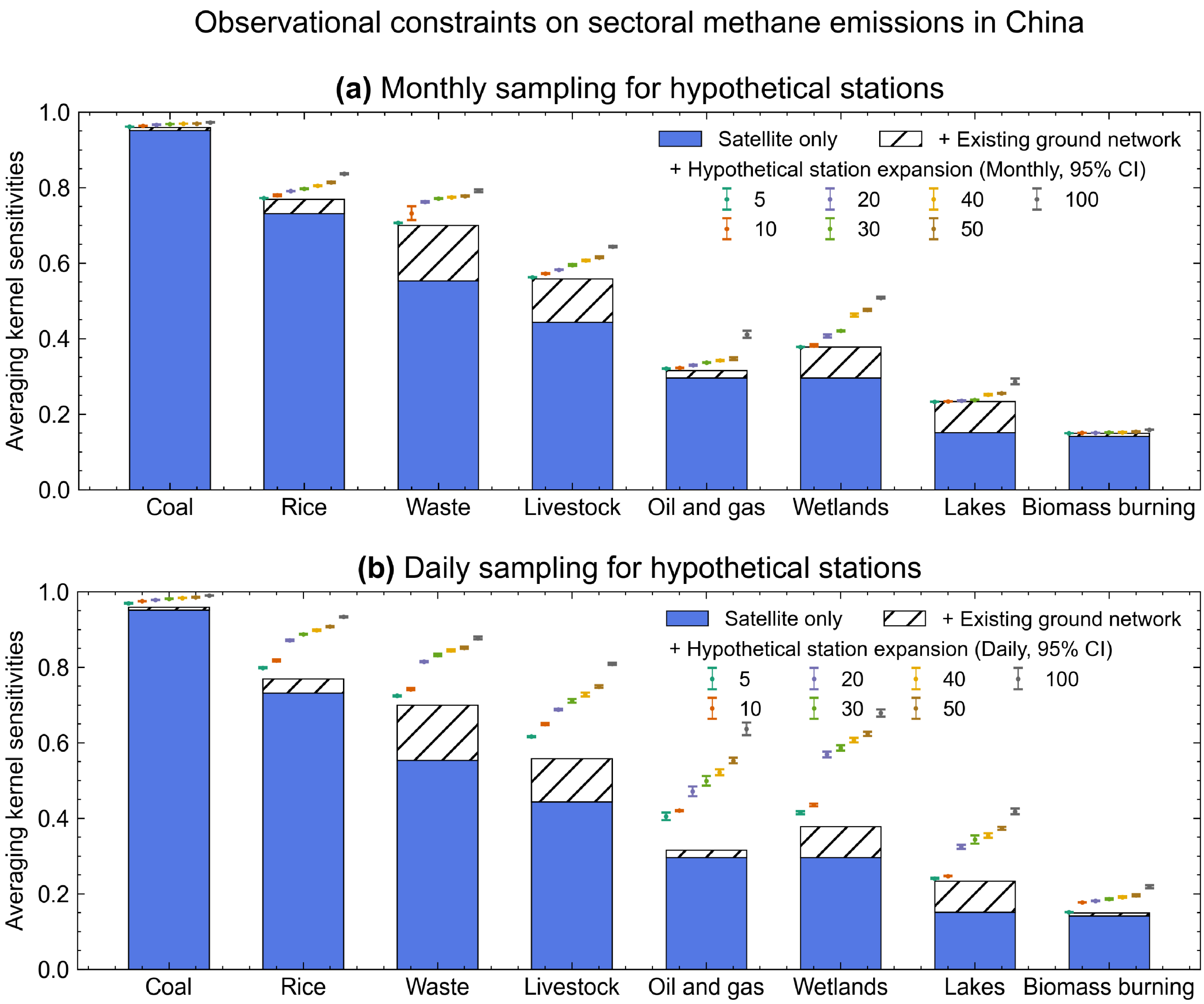

Figure S10. Observational constraint on sectoral methane emissions in China under different observational networks. Panel **(a)** shows results for hypothetical stations with monthly sampling frequency, and panel **(b)** shows results for hypothetical stations with daily sampling frequency. The blue bars represent AK sensitivities derived from TROPOMI observations alone, while the hatched bars represent the increase in AK sensitivities achieved by incorporating the existing ground-based measurements. Colored error bars show the mean AK sensitivities and 95% confidence interval (95% CI) from 10 simulated annealing experiments.

Table S1. Variables used in the K-means clustering algorithm for aggregating the low emission gridcells (< 1 Gg a^{-1}).

Category	**Input variables**	**Processing**	**Description**
Spatial coordinates	Latitude, longitude	Normalized to the range of 0–1.	To aggregate geographically proximate grid cells.
Sectorial emissions	10 Sector-specific emissions (e.g. Coal, oil, gas, livestock, rice etc.)	Normalized and weighted by sector contribution.	To group cells with similar emission-source profiles.

References

Ferrario, F. M., Crippa, M., Guizzardi, D., Muntean, M., Schaaf, E., Vullo, E. L., Solazzo, E., Olivier, J., and Vignati, E.: EDGAR v6.0 Greenhouse Gas Emissions, 2021.

Fung, I., John, J., Lerner, J., Matthews, E., Prather, M., Steele, L. P., and Fraser, P. J.: Three-dimensional model synthesis of the global methane cycle, J. Geophys. Res., 96, 13033–13065, https://doi.org/10.1029/91JD01247, 1991.

Johnson, M. S., Matthews, E., Du, J., Genovese, V., and Bastviken, D.: Methane emission from global lakes: new spatiotemporal data and observation-driven modeling of methane dynamics indicates lower emissions, J. Geophys. Res. Biogeosci., 127, e2022JG006793, https://doi.org/10.1029/2022JG006793, 2022.

Ma, S., Worden, J. R., Bloom, A. A., Zhang, Y., Poulter, B., Cusworth, D. H., Yin, Y., Pandey, S., Maasakkers, J. D., Lu, X., Shen, L., Sheng, J., Frankenberg, C., Miller, C. E., and Jacob, D. J.: Satellite constraints on the latitudinal distribution and temperature sensitivity of wetland methane emissions, AGU Adv., 2, e2021AV000408, https://doi.org/10.1029/2021AV000408, 2021.

Scarpelli, T. R., Jacob, D. J., Grossman, S., Lu, X., Qu, Z., Sulprizio, M. P., Zhang, Y., Reuland, F., Gordon, D., and Worden, J. R.: Updated global fuel exploitation inventory (GFEI) for methane emissions from the oil, gas, and coal sectors: evaluation with inversions of atmospheric methane observations, Atmos. Chem. Phys., 22, 3235–3249, https://doi.org/10.5194/acp-22-3235-2022, 2022.